Accuracy assessment of an internal resistance model of Li-ion batteries in immersion cooling configuration

Elie Solai, Ulrich Bieder, Heloise Beaugendre, Pietro Marco Congedo

Accuracy assessment of an internal resistance model of Li-ion batteries in immersion cooling configuration

Elie SOLAI[a,*], Héloïse BEAUGENDRE[a], Ulrich BIEDER[b], Pietro Marco CONGEDO[c]

[a] *Inria, Univ. Bordeaux, CNRS, Bordeaux INP, Institut de Mathématiques de Bordeaux, Bordeaux, 33000, France*
[b] *DES-STMF, CEA, Université Paris-Saclay, F-91191 Gif-sur-Yvette, France*
[c] *Inria, CMAP, CNRS, Ecole Polytechnique, IPP, Palaiseau, France*

Abstract

Internal resistance is a critical parameter of the thermal behavior of Li-ion battery cells. This paper proposes an innovative way to deal with the uncertainties related to this physical parameter using experimental data and numerical simulation. First, a CFD model is validated against an experimental configuration representing the behavior of heated Li-ion battery cells under constant discharging current conditions. Secondly, an Uncertainty Quantification based methodology is proposed to represent the internal resistance and its inherent uncertainties. Thanks to an accurate and fast to compute surrogate model, the impact of those uncertainties on the temperature evolution of Li-ion cells is quantified. Finally, Bayesian inference of the internal resistance model parameters using experimental measurements is performed, reducing the prediction uncertainty by almost 95% for some temperatures of interest. Finally, an enhanced internal model is constructed by considering the state of charge and temperature dependency on internal resistance. This model is implemented in the CFD code and used to model a full discharge of the Li-ion batteries. The resulting temperature evolution computed with the two different resistance models is compared for the low state of charge situations.

Keywords: Lithium-ion batteries, Numerical simulation, Uncertainty quantification, Surrogate model, Kriging, Bayesian calibration, Immersion cooling

*Corresponding author
Email address: elie.solai@inria.fr (Elie SOLAI)

Variables	units	
$\mathbf{u}$	[m$\cdot\ s^{-1}$]	Velocity field in fluid domain
T	[K]	Temperature field
p	[Pa]	Pressure field in fluid domain
t	[sec]	Time
$R(T)$	$[m\Omega]$	Internal resistance model function of temperature
I	[A]	Electrical current intensity
q_g	$[W \cdot m^{-2}]$	Heat source term in solid equation
C_p	$[J \cdot (kg \cdot K)^{-1}]$	Specific heat
d	[mm]	Diameter of the Li-ion cells
h	[mm]	Height of the Li-ion cells
SOC	[1]	State of charge
$\mathbf{R} = [R_0, ..., R_i, ..., R_3]$	$[m\Omega]$	Resistance vector, surrogate model input
$\mathbf{T} = [T_0, ..., T_j, ..., T_k]$	[K]	Vector of temperatures, surrogate model output
$\mathbf{T}^{exp}$	[K]	Vector of experimental measured temperature
Special characters		
ν	$[m^2 \cdot s^{-1}]$	Kinematic viscosity
ρ	$[kg \cdot m^{-3}]$	Density
λ	$[W \cdot (mK)^{-1}]$	Thermal conductivity
$\alpha = \lambda / \rho C_p$		Thermal diffusivity
$\Omega, \Omega_f, \Omega_s$		Computational domains
N_{LHS}		Number of simulations in the design of experiment
N_{MC}		Number of Monte Carlo evaluations
$\mathcal{E}_{L2}$		L2 error function
f^K		scalar output surrogate model (L2 error)
$\mathcal{M}^K$		Multiple output surrogate model
$\mathcal{X}_{DOE}$		Design of experiment for multiple output surrogate construction
$\mathcal{X}_{DOE}^{val}$		Design of exp. for validation
$\mathcal{X}_{DOE}^{\mathcal{E}_{L2}}$		Design of exp. for L2 error surrogate
$\mathcal{U}$		Uniform distribution
$\mathcal{N}$		Gaussian distribution
$\pi[X]$		Probability density function of random variable X
$\mathbb{E}$		Statistical mean
$\mathbb{V}$		Statistical variance
$\mathcal{X}_{exp}$		Design of exp. for resistance field kriging
$\hat{R}$		Kriging predictor for resistance field
$\mu_{\hat{R}}$		Mean of kriging predictor
$\sigma^2_{\hat{R}}$		Variance of kriging predictor
P_{53}		Fitting polynomial
Subscripts		
$_f$		fluid domain properties respectively
$_s$		solid domain properties
$_i$		fluid/solid interface properties

Table 1: List of notations

1. Introduction

The widespread use of electric vehicles forces manufacturers to build high-performance cars and provide the ability of fast charging for consumers. High-intensity currents demanded by these capabilities can generate intense heat loads on the battery pack of the vehicle [1]. Operating the car and battery pack under high temperatures can seriously damage the Li-ion batteries and reduce the lifespan of the whole system [2]. Then, industrial efforts are focused on Battery Thermal Management System (BTMS) to keep the batteries in a safe range of temperature during charging and discharging sequences. Those systems exist in different configurations. The most commonly used techniques include phase change material, indirect and direct fluid cooling systems [3]. So far, the immersion cooling technology seems to be the most effective solution in terms of heat transfer performances [4]. In this configuration, the cells are immersed in direct contact with the cooling fluid, either air or a dielectric liquid. The fluid crosses the Li-ion cells arrangement under forced convection regime and retrieve the heat they produce. To simulate the thermal and fluid characteristics of such systems, the classical approach is to use Computational Fluid Dynamics models. The conjugate heat transfer simulation is usually performed in 2D or 3D geometries, at transient or steady regimes. The heat equation is solved in the solid domain representing the Li-ion cells. The Navier-Stokes and energy equations are solved in the fluid domain. Continuity of temperature and heat flux are applied at the interface of both domains. The capabilities offered by CFD allow to study different features of BTMS. A 2D CFD conjugate heat transfer model is validated with experimental results for an original thermal management method using reciprocating air flow in [5]. The CFD can also be used to assess the resulting heat transfer coefficient of the fluid involved in the conjugate heat transfer [6]. The authors in [7] and [8] use 3D CFD computations to predict hot spots formation in the fluid domain depending on the Li-ion cells arrangement. Some analytical models can be developed for this configuration as in [9]. The results of their analytical method are compared with steady Finite Elements simulations.

The resulting temperature prediction in such complex simulations is strongly dependent on the heat generated by the Li-ion cells. Understanding and predicting the internal thermal behavior of Li-ion cells is then crucial to represent these systems. Electro-chemical reactions are responsible of the useful energy production by the Li-ion batteries, and then of the consequent heat generation [10, 11].

Many works try to address the simulation of the heat source within Li-ion batteries. Several approaches are performed in literature, depending on the physical scale considered. Some authors are coupling the electro-chemical equations to the thermal equations in order to represent the electronic and ionic transfer phenomenon between the layers composing the battery [12, 13, 14, 15]. Then the heat generated by these transfers is taken into account in the heat equation and then the temperature distribution in the cell is computed.

Other references consider a simpler approach for the heating source term. Indeed, solving the partial differential equations system governig the electrochemical processeses might be costly, especially if the objective is to represent a full size BTMS and solve the heat and flow equation in the whole system. Then, the challenge is to take a source term for heat equation that represents the internal phenomena occurring within the Li-ion batteries. A model taking into account two main electro chemical phenomena was first proposed by [16] and used in numerous references [17, 18, 19, 20, 7, 21, 22, 23]. According to this approach, the heat source is the result of two contributions. The first one is the heat generated by the entropy changes caused by the electrochemical reactions. The second contribution is the

heat generated by the Joule effect. It is caused by the electrons transfer across the layers composing the battery. Each of these layer present an inherent electric resistivity, and create an obstruction to the electrons motion. The induced energy loss are then released under the form of heat. Many references consider that the most part of the heat is due to the Joule effect [19, 2, 7, 5]. Using this assumption, the parameters to consider are the internal resistance and the input electrical current. The internal resistance depends on parameters such as temperature, state-of-charge of the cell and their combined effect, following relationships hard to assess in practice. Developing an accurate model to represent its behavior is a challenging topic and different methods has been tested in literature for this purpose [20, 24, 25].

In this work, only the heat produced by the Joule effect through the values of internal resistance and electric current is considered. An internal resistance model is constructed, considering its dependence on temperature only as a first assumption. We perform a 2D simulation of the conjugate heat transfer in a small battery pack immersed in air. The uncertainties coming from the internal parameters are considered thanks to the parameterization of the model. A novel methodology is presented to improve the numerical solver's temperature prediction using uncertainty quantification methods and experimental measurement. Specifically, a Bayesian inverse problem is solved and gives the calibrated distributions of the resistance model parameters leading to the model response the closest to the experimental data. Finally, for further investigation, we propose a method to build an alternative internal resistance model, dependent on both the state of charge and temperature. This model allows assessing the effect of the state of charge on the temperature evolution.

The article is divided as follows. The section 2 presents the experimental setup reproduced with the CFD model. The code TrioCFD [26] is validated for the first time in literature against an experimental configuration of Li-ion cells. In section 3 the uncertainties of the internal resistance of Li-ion cells are modeled and propagated through the CFD solver. We then assess their impact on the temperature evolution of the Li-ion cells under constant discharging conditions. Then, in section 4 deterministic and Bayesian calibrations of the internal resistance model parameters are performed using experimental measurements. The variance reduction in the temperature prediction allowed by the Bayesian inversion is quantified. Finally, the section 5 proposes a method to construct an internal resistance model considering the mixed effect of the state of charge and the temperature. The model is constructed from experimental measurements of resistance. A fitting method known as Kriging is proposed to construct a smooth and realistic model from these sparse data, considering the uncertainties in the model construction. This new model is implemented in the CFD solver and significantly impacts the temperature prediction compared to the first model with temperature dependence only.

2. Experimental and CFD test case

2.1. Experimental test case

The experiment reproduced in this study is taken from [21]. The set-up consists in two parallel rows of four Li-ion cells each (see Fig. 1). The Li-ion cells used in the experiment are cylindrical 26650 cells, with LiFePO4 chemical composition. A battery pack, composed of two rows of cells, is between enclosure walls made of plexiglass. Each cell present a diameter of $d = 25.85$ [mm] and height of $h = 62.5$ [mm], with a given spacing between cells illustrated in Fig. 1. A constant discharging electric current is applied to the Li-ion cells during the whole experiment time. According to the discharge rate of 1.5 [C], the current across the entire battery pack is set to $I = 6.9$ [A]. This discharge current is applied to the cells from the beginning of the experiment, at time $t_0 = 0$ [sec] until the final time $t_f = 1600$ [sec].

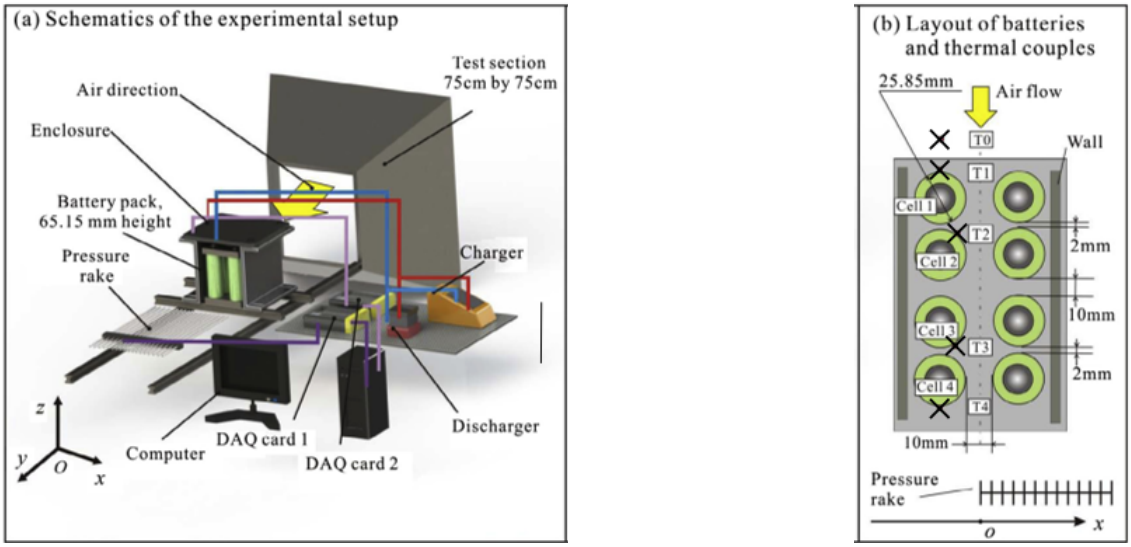

(a) (b)

Figure 1: Experimental set up. Figure courtesy of He et al. (2014) in *the International Journal of Heat and Mass Transfer*, vol. 72 [21].

The purpose of the experiment is to monitor the temperature evolution of the heated Li-ion cells measured at key locations of each cell surface. The probes positions are represented by the black cross on Fig. 1b. In this experiment, the temperature evolution of the cells is studied under various airflow conditions. The case of forced convection with a non zero inlet velocity in the fluid domain, is treated, for numeric validation purposes. Then, the uncertainty quantification study on the internal resistance model is performed in the case of pure heating of the cells, with no air inlet velocity. One scope of the present work is to consider the data coming from the experiment with the uncertainties related to the measured quantities of interest and with the inherent uncertainties of physical parameters involved in Li-ion cell heating.

2.2. Governing equations and CFD model

To represent numerically the experimental case, a two-dimensional simulation of the transient conjugate heat transfer is performed. The computational domain Ω is divided in two

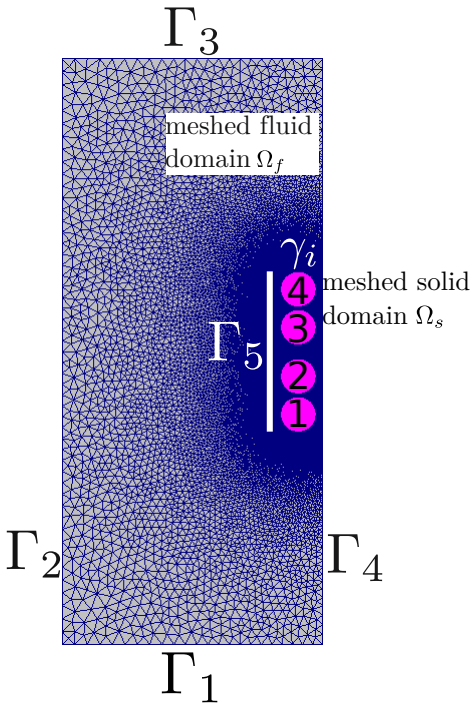

Figure 2: Mesh, computational domains and boundary labels for the CFD simulation.

sub-domains: the fluid domain and solid domain. Because of the symmetry of the experimental set-up the full domain Ω represents only half of the physical set up, namely, one plexiglass wall and only one row composed of four cells, like shown in Fig. 2.

In the fluid domain Ω_f, the Navier-Stokes equations are solved along with the energy equation. The set of equations in the fluid domain reads:

$$\begin{cases} \nabla \cdot \mathbf{u} & = & 0 \\ \frac{\partial \mathbf{u}}{\partial t} + \mathbf{u} \cdot \nabla \mathbf{u} & = & \nabla \cdot (\nu_f \nabla \mathbf{u}) - \frac{1}{\rho_f} \nabla p \\ \frac{\partial T}{\partial t} + \mathbf{u} \nabla T & = & \nabla \cdot (\alpha_f \nabla T) \end{cases} \tag{1}$$

The solid domain Ω_s represents the four heated cells. The heat equation is solved in this part of the domain. The heat equation in Ω_s reads:

$$\frac{\partial T}{\partial t} = \nabla \cdot (\alpha_s \nabla T) + \frac{q_g}{\rho_s C_{p,s}} \tag{2}$$

At the interface γ_i between the two domains Ω_f and Ω_s, the coupling conditions related to conjugate heat transfer are applied: temperature and heat flux continuity. Let's denote $T_{f,i}$ and $T_{s,i}$ the temperature on the interface in the fluid and solid domains respectively. Similarly, $\Phi_{f,i}$ and $\Phi_{s,i}$ are the heat flux coming out of the fluid and solid domain respectively. For any instant t of the simulated time, the temperature and heat flux continuity are expressed by:

$$T_{f,i} = T_{s,i} \qquad \Phi_{f,i} = -\Phi_{s,i} \tag{3}$$

The source term in the solid domain Ω_s represents the heat generated by the Joule effect, due to the discharge current I applied to the cells, and their internal resistance R. The

details about the source term expression are explained further in the article. However, to complete the equations' description, the expression of the source term in Eq. (2) is given by:

$$q_g \propto R(T) \cdot I^2 \tag{4}$$

q_g being a volumic source term, it is applied to each mesh element of the solid domain. Then the resistance depends on the temperature evaluated in each element of the discretized solid domain. The numerical tool used to solve the governing equations is TrioCFD [26], which is a numerical tool developed at CEA for heat transfer and fluid problems oriented towards nuclear applications. Note that TrioCFD is applied here for the first time in litterature to the simulation of battery cells. The conditions on the different boundaries indicated in Fig. 2 are the following ones: Γ_1 imposed temperature and velocity, Γ_2 symmetry and adiabatic for thermal equations, Γ_3 free outlet, Γ_4 symmetry, Γ_5 wall condition, γ_i coupling conditions (fluid/solid interface). TrioCFD provides the predicted temperature evolution at the probes locations showed in Fig. 1b.

2.3. Evaluation of the numerical schemes

The purpose of this section is to make sure that the numerical schemes used to solve flow and thermal equations in TrioCFD are consistent with an already validated numerical tool on this kind of heat transfer problems. A code to code comparison is performed, between TrioCFD and the code used in [21], FLUENT. The test case is set up with the following conditions: an air flow of $\mathbf{u} = 1$ [m/s] is imposed at the inlet boundary. The heat from solid domain is provided by a constant source term $q_g = 6.666 \cdot 10^3$ [W/m^2] in Eq. (2). For this case of forced convection with inlet velocity, a Low-Re $k - \varepsilon$ turbulence model [27] is added to Eq. (1). The 2D mesh contains $1.7 \cdot 10^4$ nodes. The temperature evolution is computed at the probes positions, specified in Fig. 1b. As the two numerical codes are set with the same heating conditions and the computation is made on the same mesh, it's assumed that if TrioCFD reproduces the same temperature evolution as FLUENT, the flow and heat equations are numerically solved with good consistency.

Fig. 3 shows the temperature evolution at the probes position computed by TrioCFD and FLUENT. Both codes give similar temperature prediction. Thus, from these results, confidence is gained about the numerical settings chosen for the case and the ability of TrioCFD to compute conjugate heat transfer in a case of heated Li-ion cells.

2.4. CFD simulation for the case of no inlet velocity: resulting temperature field

Here a simulation in the case of pure heating is presented, i.e. with air velocity set to $\mathbf{u} = 0$ [m/s] at inlet boundary. A Dirichlet boundary conditions is applied to the temperature of the inlet boundary: $T_{inlet} = 295.2$ [K]. The same value is used for the initial condition in the whole domain. An adiabatic wall condition is applied to symmetry boundaries for the temperature. The mesh used is the same as the one validated in the previous section, in Fig. 2.

This representation of the temperature field in Fig. 4 highlights the process of transient conjugate heat transfer. The heat is generated in the solid domain Ω_s with the volumetric heat source q_g from Eq. (4). Then the heat is spread through the solid domain in Fig. 4b, according to the conduction equation Eq. (2). The fluid in Ω_f surrounding the solid domain is retrieving the heat generated through the coupling conditions in Eq. (3). The air temperature and resulting flow is computed with Eq. (1). The air temperature in the fluid

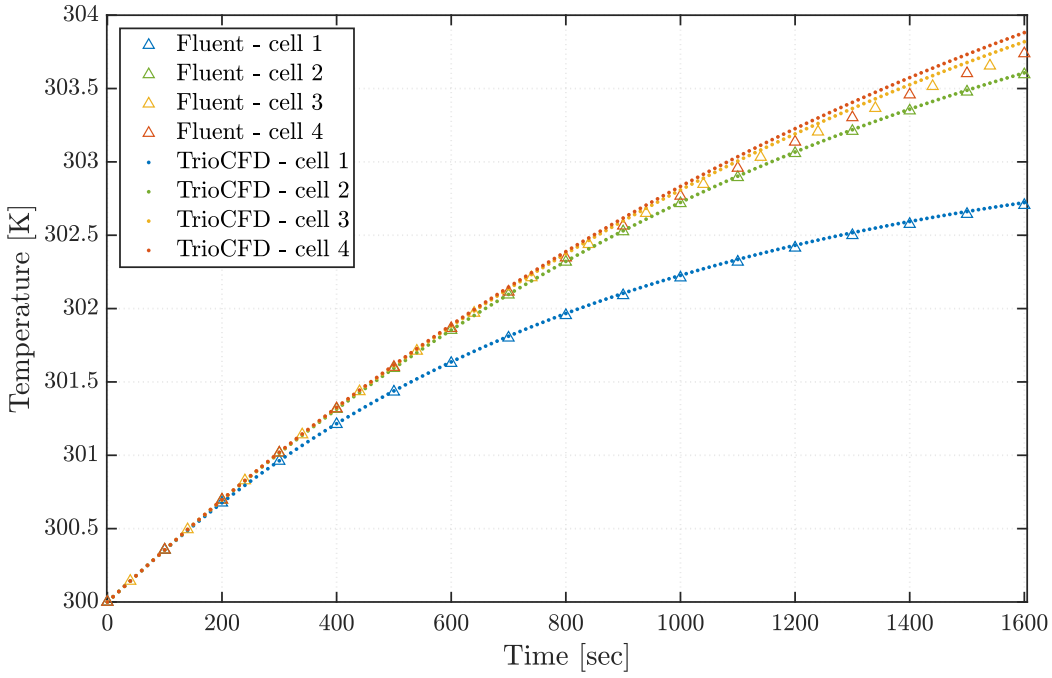

Figure 3: Numerical temperature prediction from FLUENT and TrioCFD at the probes positions, for each battery cell.

domain evolution is visible from Fig. 4a. Also, because of the cell arrangement and the wall on the left side, increased heat loads for the cells 2 and 3 are visible in Fig. 4b. This kind of thermal behavior is expected regarding the geometry of the experimental setup. Then, this simple configuration underlies the issues of thermal distribution in real battery packs where several Li-ion cells are arranged close to each other. The hereto numerical model is able to reproduce such phenomenon.

3. Modeling uncertainties in internal resistance model

Now that the description and ability of the CFD model to solve the problem of heated cells has been shown, the focus is set on studying the uncertainties related to the internal resistance model.

3.1. A priori choice of the internal resistance model

To consider uncertainties in the internal resistance values, it is first required to choose an a priori structure for the model to represent this function. From many references studying properties of Li-ion batteries, it is a good guess to assume that the internal resistance is dependent on the temperature only, in a cubic polynomial form [19, 7]. The objective here is then to build a direct relationship between the resistance of the cell and its temperature, following some physical constraints, *i.e.* $T \mapsto R(T)$. Specifically, the built model $R(T)$ is imposed to be strictly decreasing within the temperature range of the experiment following several works [19, 20, 24].

A Bezier parametrization is chosen to model the resistance, requiring the definition of some control points. Note that expected monotonic behavior of the resistance can be natu-

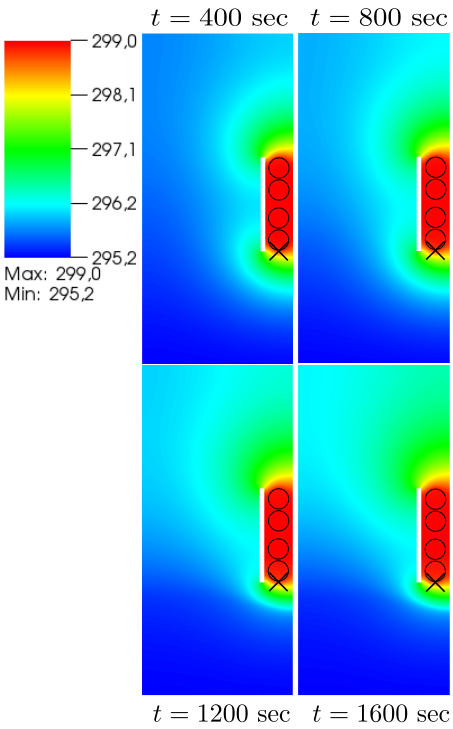

(a) Temperature fields in solid and fluid domains evolution

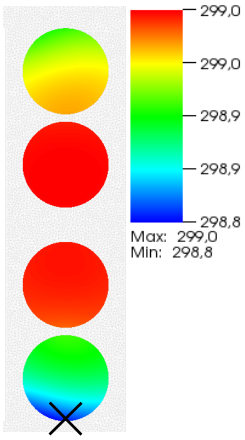

(b) Temperature field of solid domain at $t = 1600$ sec

Figure 4: (a) Contour plot of the temperature field evolution in solid and fluid domains. (b) Focus on the temperature field in the solid domain at $t = 1600$ [sec]. The black cross represents the location where the experimental data is measured.

rally imposed with a suitable choice of the control points. Within the range of relevant temperatures with respect to usual Li-ion cells problems, four values of temperature are selected, equally spaced, as input values. Then, for these selected temperature values, four corresponding values of internal resistance are taken. This process outcomes in four temperature-resistance control points. Then, the model is built using a Bezier curve parametrization. The four points $\{(T_0, R_0), ...(T_3, R_3)\}$ define the Bezier curve representing the $R(T)$ the model. An illustration of the Bezier parametrization in modelling the resistance $R(T)$ is given in Fig. 5 with five curves and their associated control points (corresponding to the same colour), within the range of temperature of the experiment represented by the vertical red dotted lines. Note that the mathematical behavior of each model is controlled through the variability of the control points. Practically, a direct relationship is established from the selected Bezier points and the explicit expression of the polynomial model $R(T)$ [28].

3.2. Uncertainty characterization of the internal resistance model

Using the Bezier parametrization, the uncertainties of the internal resistance can be represented by modelling the distribution of the control points variability. In practice, a random variable R_i is introduced, giving the resistance value at the temperature abscissa $T_i, i \in [0, 3]$ of each control point. Excepted the physical constraints detailed right above, no a priori information is known on the behavior of the model. For this reason, the introduced random variables R_i are assumed to follow an uniform distribution. A physically sound interval of variation is considered from which the resistance values can be obtained by sampling the

random variables following the uniform distribution:

$$R_i \sim \mathcal{U}([R_i^{min}, R_i^{max}]) \quad \text{for} \quad i = 0, ..., 3 \tag{5}$$

For one sampled vector of resistance values $\mathbf{R}^{(k)} = [R_0, ..., R_3]$ the corresponding Bezier polynomial model $R^{(k)}(T)$ is built and ready to be implemented in the CFD code through the source term q_g from Eq. (2).

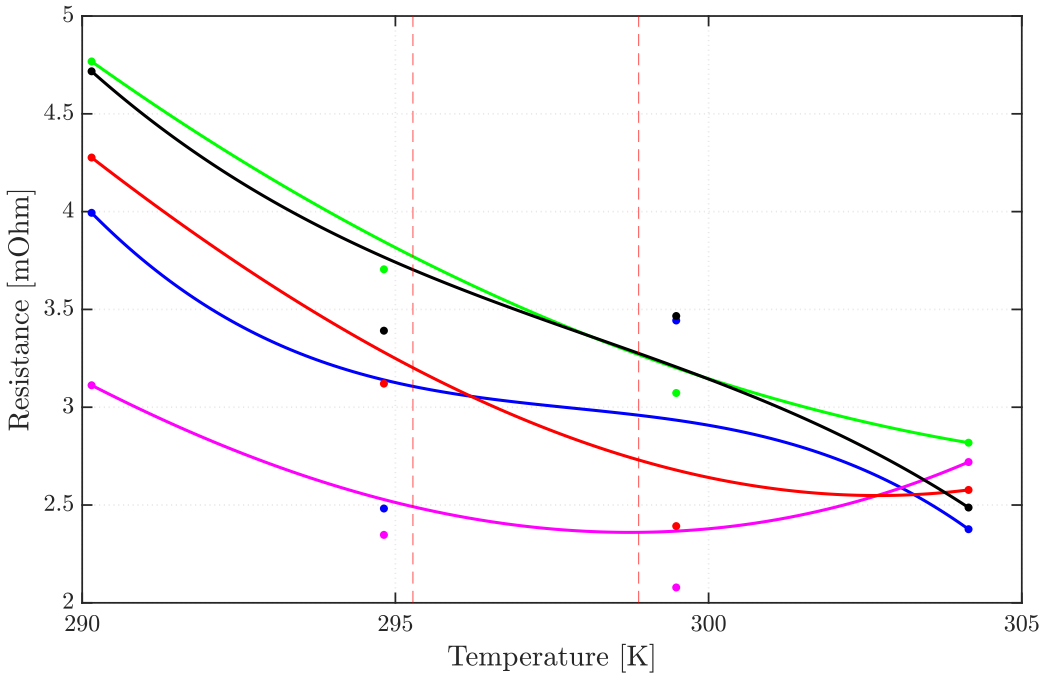

Figure 5: Five samples of the Bezier control points and corresponding $R(T)$ curves (matched by colors). The red dotted lines represent the temperature range of the experiment. The four abscissa of the control points are: $T_0 = 290$ [K]; $T_1 = 294.8$ [K]; $T_2 = 299.5$ [K]; $T_3 = 304.1$ [K]

4. Calibration of the resistance model parameters using experimental data and surrogate model

4.1. Surrogate model and uncertainty propagation

Using the process detailed in the previous section the uncertainties inherent to the internal resistance model can be modeled. The goal of this study is to assess the impact of the $R(T)$ model shape on the temperature evolution computed by the numerical model. From the uncertainty quantification perspective, the objective is to assess the impact of these uncertainties on the temperature response of the heated Li-ion battery cells.

A so-called Uncertainty propagation problem consists in propagating the input uncertainties through the numerical solver to compute a statistical distribution of a specific quantity of interest. The target here is the computation of some statistics of the temperature evolution on the Li-ion cells surface.

The statistics of interest are here the mean and variance of the temperatures T_j at fixed times t_j of the experiment. A simple approach to compute these statistics is the Monte Carlo method. The expressions of the mean $\mathbb{E}[\cdot]$ and variance $\mathbb{V}[\cdot]$ for each output T_j reads:

$$\begin{aligned} \mathbb{E}[T_j] &= \frac{1}{N_{MC}} \sum_{k=1}^{N_{MC}} T_j^{(k)} \\ \mathbb{V}[T_j] &= \frac{1}{N_{MC}} \sum_{k=1}^{N_{MC}} \left(T_j^{(k)} - \mathbb{E}[T_j] \right)^2 \end{aligned} \tag{6}$$

This method is very effective but expensive, though. In fact, it requires the evaluation of many samples N_{MC} to converge properly, which correspond in this case to many CFD expensive evaluations. Many values of the temperature response are required, each corresponding to an evaluation of the computational model with an internal resistance model $R^{(k)}(T)$ as input. This turns to be prohibitive with the present CFD model which presents a high computational cost.

The approach followed here is then to build a surrogate model of the quantity of interest as a function of the input parameters, which can be used instead of evaluating the CFD model. Practically, let's define for the surrogate model the input as a vector of four sampled values of resistance $\mathbf{R} = [R_0, ..., R_3]$. The output is represented by a vector $\mathbf{T}$ of k temperature values $\tilde{T}_k$, at different times of the experiment t_k, at the location specified in Fig. 4, such that $\tilde{T}_k = \tilde{T}(t_k)$. The surrogate model just defined is described in Eq. (7):

$$\begin{aligned} \mathcal{M}^K : \mathbb{R}^4 &\rightarrow \mathbb{R}^k \\ \mathbf{R} &\mapsto \mathbf{T} \end{aligned} \tag{7}$$

The construction of this function is performed using the Gaussian process regression theory [29, 30]. The idea is to build an interpolation function from a set of construction points constituting a so-called Design of Experiment (DOE). The built Kriging surrogate model allows to get evaluations of the quantities of interest at considerably lower computational cost.

In this case, Latin Hypercube Sampling technique (LHS) [31] was used to sample $N_{LHS} = 153$ models for the internal resistance $R^{(i)}(T), i \in [1, N_{LHS}]$. Then, a CFD simulation is

performed for each input $\mathbf{R}^{(i)}$, providing the output vector of temperature values $\mathbf{T}^{(i)}$. The points obtained after this process, constituting the DOE $\mathcal{X}_{DOE}$ are denoted as:

$$\mathcal{X}_{DOE} = \left\{ \left(\mathbf{R}^{(i)}, \mathbf{T}^{(i)} \right) \ , \ i = 1, ..., N_{LHS} \right\} \tag{8}$$

The expensive part in terms of computational cost is the construction of the DOE. Then, the computation of the statistics of interest is made possible by the N_{MC} evaluations of the surrogate model $\mathcal{M}^K$, each representing in practice roughly the cost of a vector matrix product.

Once the surrogate model is built, it is required to ensure that the surrogate model represents the numerical model with good accuracy. The Fig. 6 illustrates the evaluation of temperatures by the surrogate model for some inputs $\mathbf{R}^{(i)}$ versus the one evaluated with CFD. All the points are overlapping close to the $y = x$ line, showing an excellent accuracy of the surrogate model. In practice, an other DOE $\mathcal{X}_{DOE}^{val}$ containing $N_{val} = 82$ points, was used to perform this validation.

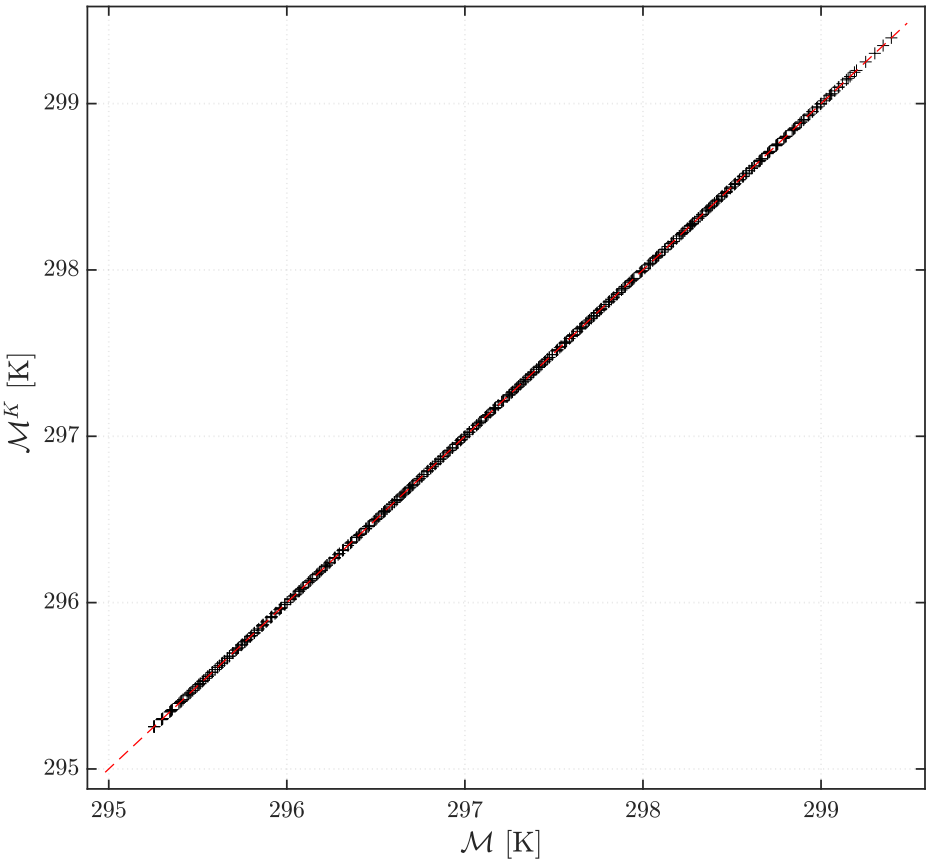

Figure 6: Comparison of surrogate model evaluations of temperature $\mathcal{M}^K$ with the CFD model $\mathcal{M}$ for given inputs $\mathbf{R}^{(i)}$. The red line represents the first bisector curve.

Since the surrogate is built, it can be utilized to compute the statistics of interest described above. Fig. 7 illustrates the surrogate model response together with the experimental data

and the CFD computation using a nominal resistance model $R_{nominal}(T)$.

The uniform prior distributions defined in the previous section are used to estimate the mean and variance of the surrogate model. The variance envelope due to the inputs uncertainties, corresponding to the 95% confidence interval in this case, overlaps with the experimental measurements and the corresponding error bars. This first result shows the interest of taking into account the input uncertainties from the resistance, compared to a deterministic approach using the CFD model and a single input resistance model. Indeed, the variability of the surrogate model response is non negligible when the prior uncertainties on the internal resistance model are considered. Furthermore, if the mean response of the surrogate model seems to be in fair agreement with the experimental measurements, the response variability is increasing with time as the temperature reaches higher values.

In the following section, the approach considered consists in using directly the experimental data to reduce this variability in the temperature prediction.

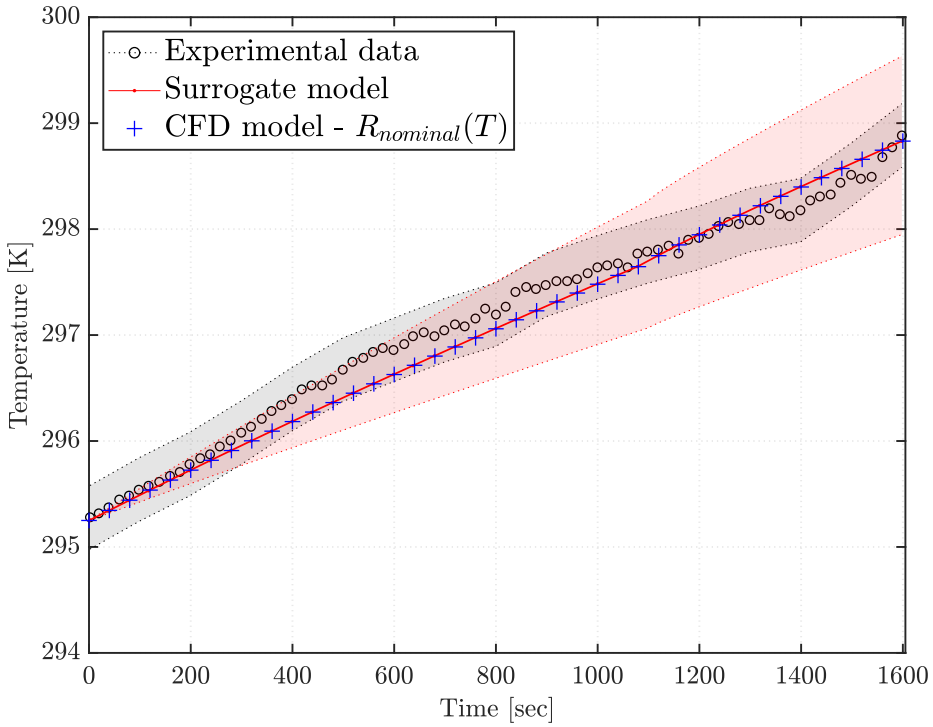

Figure 7: Surrogate model response with its variation envelope due to input prior uncertainties (red). Comparison with experimental data and its measurement error envelope (black). CFD model response with nominal input model $R_{nominal}(T)$ (blue).

4.2. Bayesian calibration of the resistance model parameters

In this section, the attention is set on the calibration of the resistance model input parameters. The first approach is to perform a deterministic calibration by minimizing the L2 error between the temperature predictions from the CFD model and the experimental measurements. The L2 error, denoted here as $\mathcal{E}_{L2}$ for a CFD run with a given input model $R(T)$ is defined by the sum of discrepancies between the temperature evaluated by the CFD model and temperature measured experimentally at each time t_j where a data is available.

$$\mathcal{E}_{L2}(R(T)) = \sum_{j=1}^{N_{exp}} \left(T^{CFD}(R(T), t_j) - T_j^{exp}\right)^2 \tag{9}$$

From the many CFD simulations in the plan of experiment, an other surrogate model f^K defined in Eq. (10) is built, mapping the values of resistance $\mathbf{R}$ with the corresponding L2 error $\mathcal{E}_{L2}$.

$$\begin{aligned} f^K : \mathbb{R}^4 &\to \mathbb{R} \\ \mathbf{R} &\mapsto \mathcal{E}_{L2} \end{aligned} \tag{10}$$

To build this surrogate model, the considered DOE is denoted as:

$$\mathcal{X}_{DOE}^{\mathcal{E}_{L2}} = \left\{ \left(\mathbf{R}^{(i)}, \mathcal{E}_{L2}^{(i)}\right) \ , \ i = 1, ..., N_{LHS} \right\} \tag{11}$$

Then a deterministic optimization problem is solved to get the values of input $\mathbf{R}$ which minimizes the function f^K. This outcomes in an optimized vector called $\mathbf{R}_{L2}$ defining a model $R_{L2}(T)$ which gives the CFD response the closest to the experimental measurements, in Fig. 8 (green). The resulting CFD computation using this input resistance model can be seen in Fig. 9 (green).

The second approach is to consider a Bayesian calibration of the parameters [32]. The objective is to compute the distribution of the input parameters $\mathbf{R} = [R_0, ..., R_3]$ conditioned to the experimental data $\mathbf{T}^{exp}$. Practically, this is the distribution of inputs leading to the model response the closest to the experimental data in a Bayesian sense. Following Bayes theorem, the relation between the posterior distribution, the likelihood, the marginal likelihood and the prior distribution reads:

$$\pi[\mathbf{R}|\mathbf{T}^{exp}] = \frac{\pi[\mathbf{T}^{exp}|\mathbf{R}] \cdot \pi[\mathbf{R}]}{\pi[\mathbf{T}^{exp}]} \tag{12}$$

where $\pi[\mathbf{R}|\mathbf{T}^{exp}]$ is the posterior distribution, $\pi[\mathbf{T}^{exp}|\mathbf{R}]$ the likelihood and $\pi[\mathbf{R}]$ the prior distribution. $\pi[\mathbf{T}^{exp}]$ is the marginal likelihood used essentially as a normalization constant.

The objective of the Bayesian calibration is to compute the posterior distribution. In this case, first, a prior distribution to the input parameters was defined in section 3.2. There is no a priori information on the input values, except an acceptable range of variation, and then a non-informative prior (uniform distribution) was chosen. The posterior distribution is computed using a Markov Chain Monte Carlo algorithm [33, 34]. The specific type of MCMC algorithm used was the Adaptive Metropolis algorithm [35, 36, 37, 38].

The resulting posterior distributions are represented in Fig. 8. The first outcome of the calibration is that the posterior distributions (red) present a narrower shape than the uninformative priors (blue). The Bayesian inverse problem actually allowed to gain information about which interval of the input values are likely to give a model response close to the experimental data. Indeed, for all of the four parameters, the posterior distributions present a single posterior mode (known as maximum a posteriori) and a low probability region (queue of the skewed distributions).

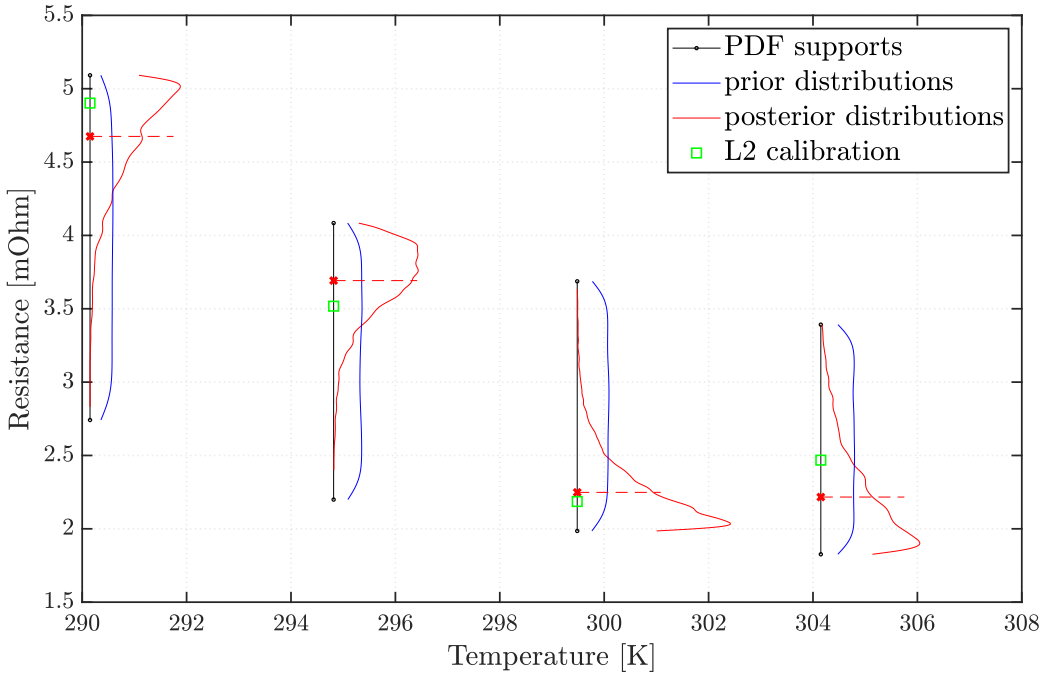

Figure 8: Prior (blue) distributions and posterior (red) distributions of input parameters after Bayesian calibration. In green, resulting values of resistance after deterministic calibration.

The posterior and prior distributions can be used to sample the input values and compute the statistics of interest defined in section 4.1. The uncertainty propagation of the input prior distributions (Fig. 8 - blue) leads to a considerable variation on the numerical prediction of temperature (Fig. 9 - blue), which envelops experimental data systematically. Considering the posterior distributions (Fig. 8 - red), the uncertainty on the input parameters has been reduced by 73%, 76%, 75%, 47% for the parameters R_0, R_1, R_2, R_3 respectively.

Furthermore, the Bayesian inference allows to gain knowledge on the numerical model response. Fig. 9, shows the temperature distributions (red) predicted by the surrogate model, resulting from the propagation of posterior input distributions in Fig. 8. It is clear that the posterior predicted distributions are more narrow than the priors. The predicted variance from prior and posterior distributions, together with the associated variance reduction are given in Tab. 2. For instance, the uncertainty for the predicted temperature at $t = 1517$ [sec] (Fig. 9) is reduced by 98% using the posterior distributions of input parameters. Also, one can note that the variance reduction gets bigger as the time increases. Indeed, the predicted variance computed from the prior is increasing significantly as the temperature increases. On the other hand, the calibrated posterior distributions allows to maintain a very small

rise of the predicted variance through time. Thus, even if the variance computed from the posteriors increase slightly, the variance reduction is increasing as the time and temperature rise. From a design point of view, this behavior is interesting since the gain of confidence in the temperature prediction is increasing over time.

In conclusion, by including the knowledge from the experimental data, the uncertainty on the model response has been reduced, and the quality of the numerical model prediction can be assessed from a more relevant perspective.

Output temperature at:	$t = 178$	$t = 377$	$t = 577$	$t = 778$	$t = 1158$	$t = 1517$
Prior predicted variance	0.001745	0.007332	0.016109	0.027687	0.057450	0.094950
Posterior predicted variance	0.000077	0.000263	0.000470	0.000667	0.001072	0.001789
Relative variance reduction [%]	95.6097	96.4173	97.0825	97.5918	98.1342	98.1154

Table 2: Predicted variance using prior and posterior distributions for some temperatures of interest at given times.

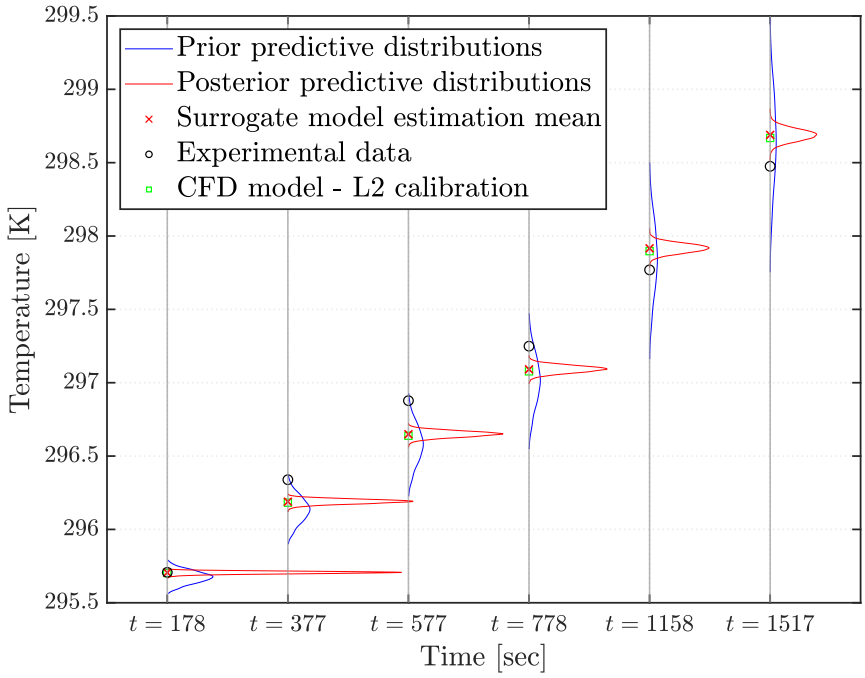

Figure 9: Prior (blue) and posterior (red) predicted distributions of the quantities of interest. In green, result of the CFD model with the $R_{L2}(T)$ input model.

5. Effect of SOC on the Li-ion cells temperature evolution

So far, only the temperature has been considered as the input variable of the internal resistance. This assumption yields convincing results in predicting temperature for experiments where a very low state of charge (SOC) is not reached. Although, the state of charge might still significantly affect the resistance value when performing full discharge cycles. This impact on the resistance value is expected to change the shape of the temporal temperature response from the heated Li-ion batteries. Many studies have proposed methods or experimental investigations to represent the effect of SOC in the model for the internal resistance [24, 39, 40, 41, 42, 43, 44]. This section proposes a method to consider the effect of SOC and build an internal resistance accordingly.

5.1. Construction of an internal resistance model from experimental measurements

From a number N_{exp} of available experimental measurements of internal resistance at different SOC and temperature values, the internal resistance model is constructed, using a Kriging parametrization [45, 46]. The experimental points (materialized by the crosses in Fig. 10 and Fig. 11) used to construct the Kriging are denoted:

$$\mathcal{X}_{exp} = \left\{ \left(SOC^{(k)}, T^{(k)}, R^{(k)} \right), k = 1, ..., N_{exp} \right\} \tag{13}$$

We obtain a Kriging predictor $\hat{R}$ which depends on the inputs $\mathbf{z} = (SOC, T)$. The parametrization of this function is made thanks to the definition of correlation functions, describing the correlated effect of two input points $\mathbf{z}$ and $\mathbf{z}'$ on the output $\hat{R}$. Then, the construction of the Kriging model consists in the optimization of coefficients (called hyperparameters) parametrizing these functions, by maximizing the likelihood of observing the construction points with the model. The Kriging predictor is a random variable indexed by $\mathbf{z}$ following a Gaussian distribution of mean $\mu_{\hat{R}}(\mathbf{z})$ and variance $\sigma^2_{\hat{R}}(\mathbf{z})$ [47].

$$\hat{R}(\mathbf{z}) \sim \mathcal{N}\left(\mu_{\hat{R}}(\mathbf{z}), \sigma^2_{\hat{R}}(\mathbf{z})\right) \tag{14}$$

Once the Kriging model is constructed, it is evaluated on a large set of test points ($N = 1 \cdot 10^4$ points) sampled following a uniform distribution, on the range of variations considered for each input variable. In Fig. 10, the mean and variance of the Kriging predictor $\hat{R}(\mathbf{z})$ are plotted. The locations where the variance is high corresponds to areas where no experimental data were available. Hence, these locations present a significant uncertainty on the resistance value, quantified by the variance.

The obtained resistance values from $\mathcal{X}_{test}$ are also visible in Fig. 11 in a 3D shape. In a nutshell, the parametrization of the internal resistance model allowed to obtain a smooth surface even with sparse data. Also, the probabilistic perspective inherent to Kriging gives a confidence interval on the values taken by the model between the construction points.

In terms of computational and implementation efforts, it is not convenient to input the Kriging predictor directly in the CFD model. Indeed, a consequent matrix inversion would be necessary to evaluate the Kriging function $\hat{R}(SOC, T)$ and compute the source term in Eq. (4) at each time step. For this reason, the surface generated by the Kriging estimator on the N points $\mathcal{X}$ is fitted with bi-variate polynomials, using least square regression. The polynomial structure is chosen a priori: a maximal degree 5 is considered for the SOC dependency, and degree 3 for the temperature. The quality of the fit is assessed, and the final analytical expression of the polynomial is provided in the Appendix.

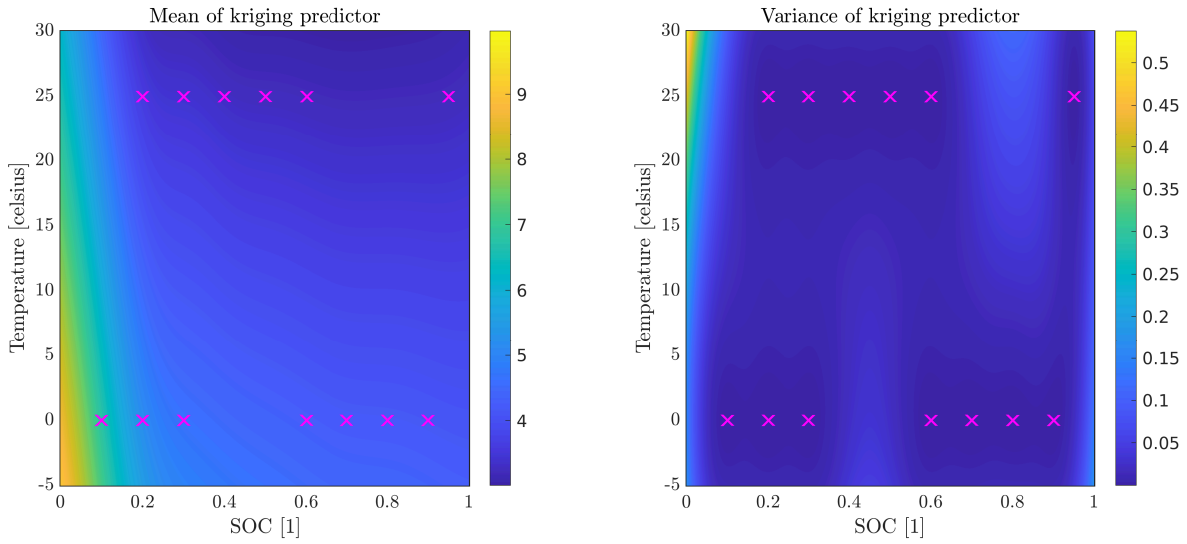

Figure 10: Mean and variance of the Kriging predictor and experimental points used for construction.

5.2. Resulting temperature evolution

The resistance model just constructed is used as a source term in the CFD solver. A simulation similar to the previous one is performed for a longer time $t_f = 2400$ [sec]. The objective is to discharge the Li-ion cells more than in the case with $t_f = 1600$ [sec] and try to observe a more significant effect of the SOC in the temperature prediction by the solver.

The results of the simulations are shown in Fig. 12. The black temperature curve is the temperature computed with the model $R_{L2}(T)$, *i.e.* the model outcoming of the deterministic optimization performed in section 4.2. The purple curve is the temperature computed with the model $R(SOC, T)$ using the P_{53} polynomial.

Because of the parametrization with polynomial P_{53}, the temperature evolution follows the trend of the curve with $R_{L2}(T)$. Indeed the resistance field is 'flat' when the SOC is still above 50%, and the effect of SOC is not significant in this zone (Fig. 11). After $t = 1000$ [sec], when the SOC goes under 55%, the slope of the temperature curve is increasing. One can notice that the temperature curves corresponding to $R_{L2}(T)$ and $R(SOC, T)$ models show different slopes from this point. After $t = 1600$ [sec], when the SOC goes under 30%, the slope is increasing even more. At the end of the simulation, when the SOC approaches 10%, the curve presents a local and high increase. The resistance value is in the steep and high-value zone of the field from Fig. 11. Then we highlighted the modified behavior of the temperature response when including the effect of SOC.

Physically, we know from data that the battery's internal resistance is degrading (significant increase) when the SOC is low. Thus, the model $R(SOC, T)$ allows assessing the impact of this degradation on the temperature evolution, which is not observable with a model depending on the temperature only.

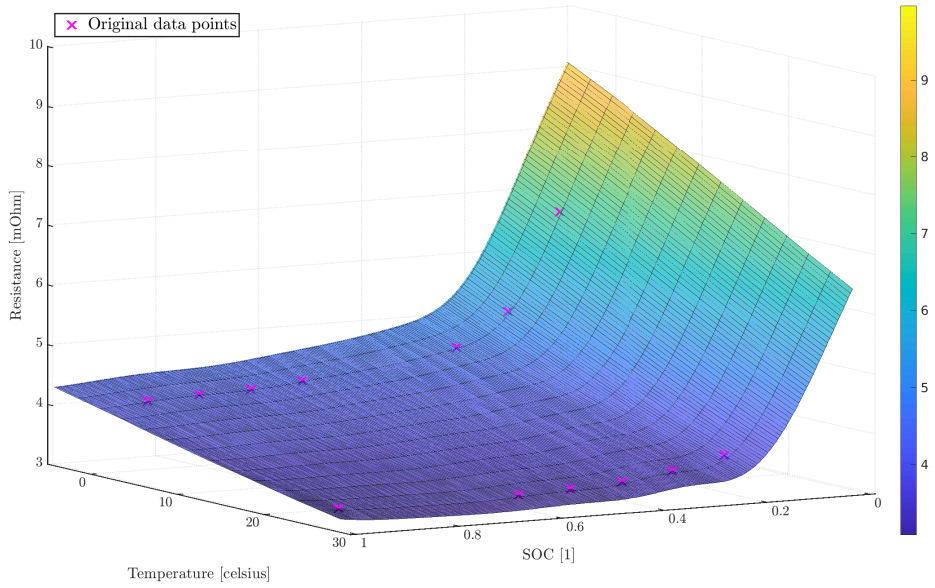

Figure 11: Kriging surface interpolating the original construction points.

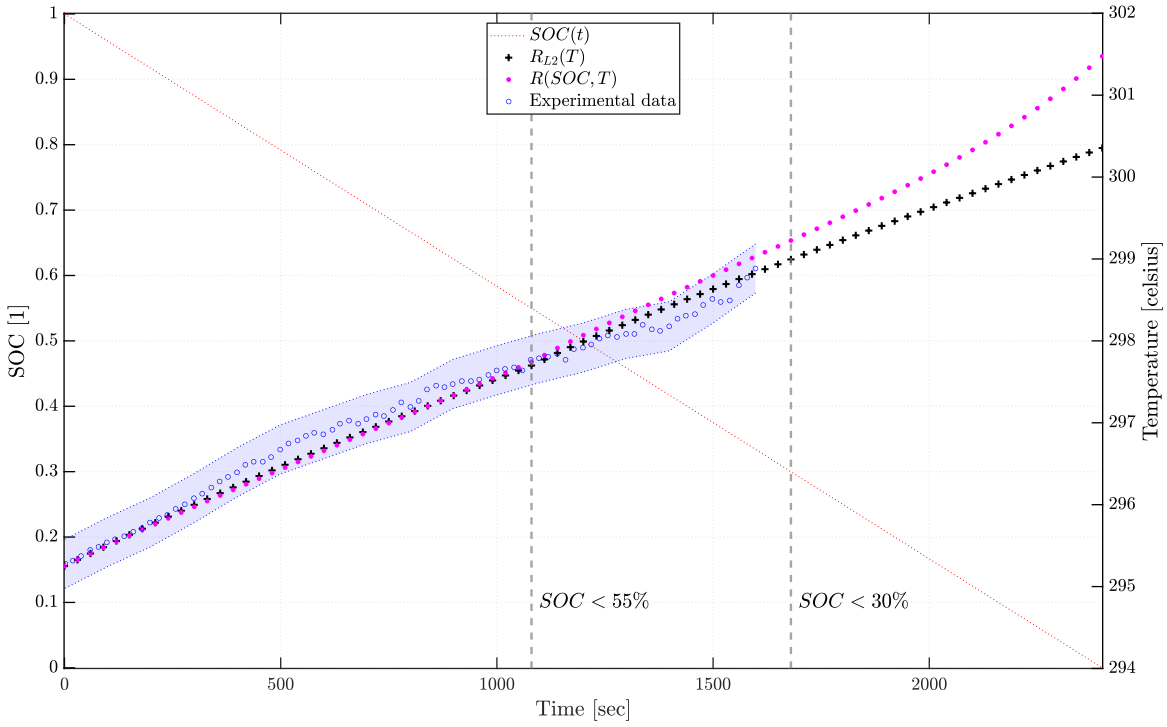

Figure 12: CFD temperature response with $R_{L2}(T)$ and $R(SOC, T)$ models.

6. Conclusion

In this study, we present an accurate simulation of Li-ion batteries under immersion cooling configuration. Specifically, we illustrate the development of an internal resistance model, mainly responsible for heat generation.

TrioCFD code is applied and validated for the first time on a Li-ion batteries heat transfer problem against experimental data from the literature, using a 2D transient conjugate heat transfer simulation. A methodology based on Bezier parameterization is proposed to build an internal resistance model dependent on the temperature only, fulfilling physical constraints acknowledged in the literature.

An accurate and fast to compute surrogate model is built to consider uncertainties associated with the parameters driving the internal resistance model. A Bayesian inverse problem is solved using the experimental measurements of temperature directly. Informative and narrow posterior distributions are obtained for the uncertain resistance input parameters. Thus, the uncertainty coming from these parameters is considerably reduced compared to the prior distribution assumed a priori. For the input parameters, this process allows reaching a maximum of 76% uncertainty reduction. These posterior distributions are propagated through the numerical model, using the surrogate model. With these informative distributions, uncertainty on temperature prediction is reduced by at least 95% all along the simulated time.

Finally, a method to enhance the internal resistance model fidelity is proposed. A resistance model considering the state of charge and temperature's combined effect is constructed based on sparse experimental data. The Kriging parametrization allows assessing the relevance of the model regarding the available data while keeping a smooth and realistic shape of the bi-variate function. The model is propagated through the CFD code, and transient simulations are performed for longer physical times. The model taking into account the effect of SOC shows a significant shape increase in the temperature prediction when the Li-ion cells reach low SOC values at the end of the discharge.

Enhancing the predictive character of this approach would require the use of the Bayesian framework, and the methodology presented here should be used to calibrate the parameters governing the bi-variate polynomial resistance model. Additional experimental measurements of batteries' temperature in full discharge cases would also be required to obtain the distributions of parameters representative of the overheating induced by the state of charge.

7. Appendix

The analytical expression of the fitted polynomial P_{53} is given by:

$$\begin{aligned} P_{53}(x,y) &= a_{00} + a_{10}x + a_{01}y + a_{20}x^2 + a_{11}xy + a_{02}y^2 \\ &+ a_{30}x^3 + a_{21}x^2y + a_{12}xy^2 + a_{03}y^3 + a_{40}x^4 \\ &+ a_{31}x^3y + a_{22}x^2y^2 + a_{13}xy^3 + a_{50}x^5 + a_{41}x^4y \\ &+ a_{32}x^3y^2 + a_{23}x^2y^3 \\ &\quad (x = SOC \;\; and \;\; y = T) \end{aligned} \tag{15}$$

Acknowledgment

This work was supported by Inria, co-funded by Inria Bordeaux Sud–Ouest and the Conseil Régional de la Nouvelle Aquitaine under Grant Agreement No 2016-1R60205-00007444-THESE. Numerical experiments presented in this paper were carried out using the PlaFRIM experimental testbed, supported by Inria, CNRS (LABRI and IMB), Université de Bordeaux, Bordeaux INP and Conseil Régional d'Aquitaine (see https://www.plafrim.fr/).

References

[1] D. Andre, S.-J. Kim, P. Lamp, S. Lux, F. Maglia, O. Paschos, B. Stiaszny, Future generations of cathode materials: An automotive industry perspective (review), Journal of Materials Chemistry A (2015).

[2] N. Sato, Thermal behavior analysis of lithium-ion batteries for electric and hybrid vehicles, Journal of Power Sources (2001) 8.

[3] M. Al-Zareer, I. Dincer, M. A. Rosen, A review of novel thermal management systems for batteries, International Journal of Energy Research 42 (10) (2018) 3182–3205. doi:10.1002/er.4095.
URL http://doi.wiley.com/10.1002/er.4095

[4] E. B. Haghighi, M. Moghaddam, Analyzing thermal management methods of li-ion battery modules, in: 2018 IEEE International Telecommunications Energy Conference (INTELEC), 2018, pp. 1–4. doi:10.1109/INTLEC.2018.8612411.

[5] R. Mahamud, C. Park, Reciprocating air flow for Li-ion battery thermal management to improve temperature uniformity, Journal of Power Sources 196 (13) (2011) 5685–5696. doi:10.1016/j.jpowsour.2011.02.076.
URL https://linkinghub.elsevier.com/retrieve/pii/S0378775311005039

[6] R. Camilleri, M. Sawani, Prediction of the Heat Transfer Coefficient in Direct Oil Cooling of Lithium-Ion Batteries, in: 2018 5th International Symposium on Environment-Friendly Energies and Applications (EFEA), IEEE, Rome, 2018, pp. 1–6. doi:10.1109/EFEA.2018.8617101.
URL https://ieeexplore.ieee.org/document/8617101/

[7] R.-D. Jilte, R. Kumar, Numerical investigation on cooling performance of li-ion battery thermal management system at high galvanostatic discharge, Engineering Science and technology, an International Journal (2018). doi:https://doi.org/10.1016/j.jestch.2018.07.015.

[8] L. Fan, J. Khodadadi, A. Pesaran, A parametric study on thermal management of an air-cooled lithium-ion battery module for plug-in hybrid electric vehicles, Journal of Power Sources 238 (2013) 301–312. doi:10.1016/j.jpowsour.2013.03.050.
URL https://linkinghub.elsevier.com/retrieve/pii/S0378775313004412

[9] D. Chalise, K. Shah, R. Prasher, A. Jain, Conjugate Heat Transfer Analysis of Thermal Management of a Li-Ion Battery Pack, Journal of Electrochemical Energy Conversion and Storage 15 (1) (2018) 011008. doi:10.1115/1.4038258.
URL https://asmedigitalcollection.asme.org/electrochemical/article/doi/10.1115/1.4038258/444019/Conjugate-Heat-Transfer-Analysis-of-Thermal

[10] M. Doyle, T. F. Fuller, J. Newman, Modeling of Galvanostatic Charge and Discharge of the Lithium/Polymer/Insertion Cell, Journal of The Electrochemical Society 140 (6) (1993) 1526–1533. doi:10.1149/1.2221597.
URL https://iopscience.iop.org/article/10.1149/1.2221597

[11] Q. Wang, B. Jiang, B. Li, Y. Yan, A critical review of thermal management models and solutions of lithium-ion batteries for the development of pure electric vehicles, Renewable and Sustainable Energy Reviews 64 (2016) 106–128. doi:10.1016/j.rser.2016.05.033.
URL http://linkinghub.elsevier.com/retrieve/pii/S1364032116301435

[12] Y. Li, Z. Zhou, W.-T. Wu, Three-dimensional thermal modeling of Li-ion battery cell and 50 V Li-ion battery pack cooled by mini-channel cold plate, Applied Thermal Engineering 147 (2019) 829–840. doi:10.1016/j.applthermaleng.2018.11.009.
URL https://linkinghub.elsevier.com/retrieve/pii/S1359431118343965

[13] L. H. Saw, Y. Ye, A. A. Tay, W. T. Chong, S. H. Kuan, M. C. Yew, Computational fluid dynamic and thermal analysis of Lithium-ion battery pack with air cooling, Applied Energy 177 (2016) 783–792. doi:10.1016/j.apenergy.2016.05.122.
URL https://linkinghub.elsevier.com/retrieve/pii/S0306261916307279

[14] D. H. Jeon, S. M. Baek, Thermal modeling of cylindrical lithium ion battery during discharge cycle, Energy Conversion and Management 52 (8-9) (2011) 2973–2981. doi:10.1016/j.enconman.2011.04.013.
URL https://linkinghub.elsevier.com/retrieve/pii/S0196890411001439

[15] S. Basu, K. S. Hariharan, S. M. Kolake, T. Song, D. K. Sohn, T. Yeo, Coupled electrochemical thermal modelling of a novel Li-ion battery pack thermal management system, Applied Energy 181 (2016) 1–13. doi:10.1016/j.apenergy.2016.08.049.
URL https://linkinghub.elsevier.com/retrieve/pii/S0306261916311369

[16] D. Bernardi, A General Energy Balance for Battery Systems, Journal of The Electrochemical Society 132 (1) (1985) 5. doi:10.1149/1.2113792.
URL https://iopscience.iop.org/article/10.1149/1.2113792

[17] W. Cao, C. Zhao, Y. Wang, T. Dong, F. Jiang, Thermal modeling of full-size-scale cylindrical battery pack cooled by channeled liquid flow, International Journal of Heat and Mass Transfer 138 (2019) 1178–1187. doi:10.1016/j.ijheatmasstransfer.2019.04.137.
URL https://linkinghub.elsevier.com/retrieve/pii/S0017931018361489

[18] Xia, Liu, Huang, Yang, Lai, Zheng, Wang, Wang, Wang, Thermal Analysis and Improvements of the Power Battery Pack with Liquid Cooling for Electric Vehicles, Energies 12 (16) (2019) 3045. doi:10.3390/en12163045.
URL https://www.mdpi.com/1996-1073/12/16/3045

[19] C. Park, A. K. Jaura, Dynamic Thermal Model of Li-Ion Battery for Predictive Behavior in Hybrid and Fuel Cell Vehicles, in: SAE Technical Paper, 2003, pp. 2003–01–2286. doi:10.4271/2003-01-2286.
URL https://www.sae.org/content/2003-01-2286/

[20] G. Karimi, X. Li, Thermal management of lithium-ion batteries for electric vehicles, International Journal of Energy Research 37 (1) (2013) 13–24. doi:10.1002/er.1956.
URL http://doi.wiley.com/10.1002/er.1956

[21] F. He, X. Li, L. Ma, Combined experimental and numerical study of thermal management of battery module consisting of multiple Li-ion cells, International Journal of Heat and Mass Transfer 72 (2014) 622–629. doi:10.1016/j.ijheatmasstransfer.2014.01.038.
URL https://linkinghub.elsevier.com/retrieve/pii/S0017931014000660

[22] N. Damay, C. Forgez, M.-P. Bichat, G. Friedrich, A. Ospina, Thermal modeling and experimental validation of a large prismatic Li-ion battery, in: IECON 2013 - 39th Annual Conference of the IEEE Industrial Electronics Society, IEEE, Vienna, Austria, 2013, pp. 4694–4699. doi:10.1109/IECON.2013.6699893.
URL http://ieeexplore.ieee.org/document/6699893/

[23] J. Kleiner, L. Komsiyska, G. Elger, C. Endisch, Thermal Modelling of a Prismatic Lithium-Ion Cell in a Battery Electric Vehicle Environment: Influences of the Experimental Validation Setup, Energies 13 (1) (2019) 62. doi:10.3390/en13010062.
URL https://www.mdpi.com/1996-1073/13/1/62

[24] Y. Li, L. Wang, C. Liao, Wu Lingfei, Li Junfeng, Guo Yanjie, Effects of temperature on dynamic characteristics of li-ion batteries in electric vehicle applications, in: 2014 IEEE Conference and Expo Transportation Electrification Asia-Pacific (ITEC Asia-Pacific), IEEE, Beijing, China, 2014, pp. 1–6. doi:10.1109/ITEC-AP.2014.6940648.
URL http://ieeexplore.ieee.org/document/6940648/

[25] Z. Wang, X. Tong, K. Liu, C.-M. Shu, F. Jiang, Q. Luo, H. Wang, Calculation methods of heat produced by a lithium-ion battery under charging-discharging condition, Fire and Materials 43 (2) (2019) 219–226. doi:10.1002/fam.2690.
URL https://onlinelibrary.wiley.com/doi/abs/10.1002/fam.2690

[26] TrioCFD, CEA.
URL https://triocfd.cea.fr/

[27] W. Jones, B. Launder, The prediction of laminarization with a two-equation model of turbulence, International Journal of Heat and Mass Transfer 15 (2) (1972) 301–314. doi:10.1016/0017-9310(72)90076-2.
URL https://linkinghub.elsevier.com/retrieve/pii/0017931072900762

[28] C. Sanchez-Reyes, Nonparametric Bezier Representation of Polynomial Transition Curves, Journal of Surveying Engineering 144 (2) (2018) 04018001. doi:10.1061/(ASCE)SU.1943-5428.0000251.
URL http://ascelibrary.org/doi/10.1061/%28ASCE%29SU.1943-5428.0000251

[29] C. Rasmussen, Gaussian Process for Machine Learning, The MIT Press, 2006, massachusets Institute of Technology.

[30] J. D. Martin, T. W. Simpson, Use of kriging models to approximate deterministic computer models, AIAA Journal 43 (4) (2005) 853–863. doi:10.2514/1.8650.
URL https://doi.org/10.2514/1.8650

[31] J. Helton, F. Davis, Latin hypercube sampling and the propagation of uncertainty in analyses of complex systems, Reliability Engineering & System Safety 81 (1) (2003) 23–69. doi:10.1016/S0951-8320(03)00058-9.
URL https://linkinghub.elsevier.com/retrieve/pii/S0951832003000589

[32] M. C. Kennedy, A. OHagan, Bayesian calibration of computer models, Journal of the Royal Statistical Society: Series B (Statistical Methodology) 63 (3) (2001) 425–464. doi:10.1111/1467-9868.00294.
URL http://doi.wiley.com/10.1111/1467-9868.00294

[33] J. S. Liu, Monte Carlo Strategies in Scientific Computing, Springer Publishing Company, Incorporated, 2008.

[34] C. Robert, G. Casella, Monte Carlo Statistical Methods. 2nd ed, Springer-Verlag, New York, 2008.

[35] H. Heikki, S. Eero, T. Johanna, An adaptive metropolis algorithm, Bernoulli 7 (2) (2001) 223–242.
URL http://www.jstor.org/stable/3318737

[36] N. Metropolis, A. W. Rosenbluth, M. N. Rosenbluth, A. H. Teller, E. Teller, Equation of State Calculations by Fast Computing Machines, The Journal of Chemical Physics 21 (6) (1953) 1087–1092. doi:10.1063/1.1699114.
URL http://aip.scitation.org/doi/10.1063/1.1699114

[37] W. K. Hastings, monte carlo sampling methods using markov chains and their applications (1970) 14.

[38] J. E. Griffin, S. G. Walker, On adaptive Metropolis–Hastings methods, Statistics and Computing 23 (1) (2013) 123–134. doi:10.1007/s11222-011-9296-2.
URL http://link.springer.com/10.1007/s11222-011-9296-2

[39] D. Ansean, M. Gonzalez, J. C. Viera, V. M. Garcia, J. C. Alvarez, C. Blanco, Electric Vehicle Li-Ion Battery Evaluation Based on Internal Resistance Analysis, in: 2014 IEEE Vehicle Power and Propulsion Conference (VPPC), IEEE, Coimbra, Portugal, 2014, pp. 1–6. doi:10.1109/VPPC.2014.7007058.
URL http://ieeexplore.ieee.org/document/7007058/

[40] L. Xiongping, Z. Jieqing, Z. Zheng, L. Feng, D. Dingrong, C. Chunyan, W. Xin, Q. Linhua, Y. Juqiong, State of Charge and Lithium Manganate Batteries Internal Resistance Estimation at Low Charge/discharge rates, International Journal of Electrochemical Science (2021) 151024doi:10.20964/2021.01.48.
URL http://www.electrochemsci.org/abstracts/vol16/16010151024.pdf

[41] C. Wu, R. Fu, Z. Xu, Y. Chen, Improved State of Charge Estimation for High Power Lithium Ion Batteries Considering Current Dependence of Internal Resistance, Energies 10 (10) (2017) 1486. doi:10.3390/en10101486.
URL http://www.mdpi.com/1996-1073/10/10/1486

[42] J. Yang, X. Wei, H. Dai, J. Zhu, X. Xu, Lithium-Ion Battery Internal Resistance Model Based on the Porous Electrode Theory, in: 2014 IEEE Vehicle Power and Propulsion Conference (VPPC), IEEE, Coimbra, 2014, pp. 1–6. doi:10.1109/VPPC.2014.7007096.
URL https://ieeexplore.ieee.org/document/7007096/

[43] D.-I. Stroe, M. Swierczynski, S. K. Kar, R. Teodorescu, A comprehensive study on the degradation of lithium-ion batteries during calendar ageing: The internal resistance increase, in: 2016 IEEE Energy Conversion Congress and Exposition (ECCE), IEEE, Milwaukee, WI, USA, 2016, pp. 1–7. doi:10.1109/ECCE.2016.7854664.
URL http://ieeexplore.ieee.org/document/7854664/

[44] L. Chen, M. Zhang, Y. Ding, S. Wu, Y. Li, G. Liang, H. Li, H. Pan, Estimation the internal resistance of lithium-ion-battery using a multi-factor dynamic internal resistance model with an error compensation strategy, Energy Reports 7 (2021) 3050–3059. doi:10.1016/j.egyr.2021.05.027.
URL https://linkinghub.elsevier.com/retrieve/pii/S235248472100305X

[45] D. G. Krige, A statistical approach to some mine valuation and allied problems on the Witwatersrand, Ph.D. thesis, Univ. of the Witwatersrand, Johannesburg (1951).

[46] M. A. Oliver, R. Webster, Kriging: a method of interpolation for geographical information systems, International journal of geographical information systems 4 (3) (1990) 313–332. doi:10.1080/02693799008941549.
URL http://www.tandfonline.com/doi/abs/10.1080/02693799008941549

[47] T. J. Santner, B. J. Williams, W. I. Notz, The Design and Analysis of Computer Experiments, 2018, Ch. 3.